JOURNAL OF SYNCHROTRON RADIATION

ISSN 1600-5775

Zernike phase-contrast full-field transmission X-ray nanotomography for 400 micrometre-sized samples

Jae Yeon Park,[a]‡ Yeseul Kim,[b]§ Sangsul Lee[a] and Jun Lim[a]*

[a]Pohang Light Source-II, Pohang Accelerator Laboratory, Jigokro 127, Pohang 36763, South Korea, and [b]Soft Matter Physics Laboratory, Sungkyunkwan University, Suwon 16419, Republic of Korea.
*Correspondence e-mail: limjun@postech.ac.kr

Received 4 March 2020
Accepted 10 September 2020

Edited by A. Stevenson, Australian Synchrotron, Australia

‡ Now at: Radiation Equipment Research Division, Korea Atomic Energy Research Institute, Jeongup 56212, South Korea.
§ Now at: Pohang Light Source-II, Pohang Accelerator Laboratory, Jigokor 127, Pohang 37673, South Korea.

Keywords: full-field X-ray microscopy; computed tomography; large field of view.

Full-field X-ray nanotomography based on a Fresnel zone plate offers a promising and intuitive approach to acquire high-quality phase-contrast images with a spatial resolution of tens of nanometres, and is applicable to both synchrotron radiation and laboratory sources. However, its small field of view (FOV) of tens of micrometres provides limited volume information, which primarily limits its application fields. This work proposes a method for expanding the FOV as the diameter of the objective zone plate, which provides a 400 µm FOV at below 500 nm resolution with Zernike phase contrast. General applications of large-volume nanotomography are demonstrated in integrated circuit microchips and Artemia cysts. This method can be useful for imaging/analyzing industrial and biological samples where bulk properties are important or the sample is difficult to section.

1. Introduction

X-ray microscopy offers complementary capabilities of optical and electron microscopy, while bridging the resolution gap between these two methods. X-ray computed tomography (CT) in particular allows the nondestructive visualization and 3D reconstruction of both the external and internal structures of an object. The easy application and powerful capabilities have enabled its widespread use in medical diagnostics, industrial testing and scientific research. However, the resolution of projection-based X-ray CT devices is limited to the micrometre scale, mainly due to the spot-size limitations of the available X-ray sources. The increasing demand for higher resolution in X-ray CT has led to the accelerated development of smaller and brighter X-ray sources (Wenz *et al.*, 2015; Larsson *et al.*, 2016). Recently, absorption-contrast X-ray CT with an ~100 nm spatial resolution has been demonstrated using an advanced X-ray source with ~250 nm spot size (Müller *et al.*, 2017; Ferstl *et al.*, 2020). Grating-based phase-contrast X-ray CT is also being actively studied in parallel to improve the contrast (Pfeiffer *et al.*, 2006). X-ray holotomography (Cloetens *et al.*, 1999; Burg *et al.*, 2020; Reichardt *et al.*, 2020; Martínez-Criado *et al.*, 2016), which takes Fresnel diffraction images at multiple propagation distances and computes a phase image, has also been recently introduced to achieve ~100 nm resolution images using a spot size of ~50 nm (Cheng *et al.*, 2014). However, such a small beam can only be realized when using coherent lights and state-of-the-art X-ray optics. Up to now, the implementation of projection-based, phase-contrast and real-space X-ray CT with a resolution of ~100 nm remains a challenge.

CT imaging with a resolution of tens of nanometres has been realized using high-brilliance synchrotron X-rays

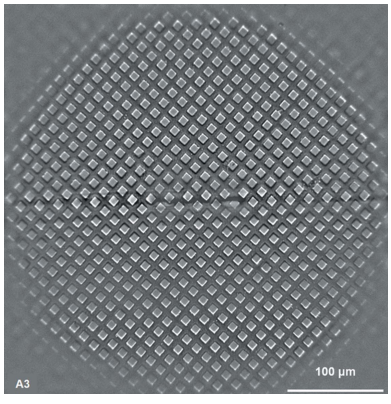

© 2020 International Union of Crystallography

combined with zone plate optics. Full-field transmission X-ray microscopy (TXM), also known as real-space microscopy, is the most popular method for capturing Zernike phase-contrast images. Currently in hard X-ray TXM-CT, the practical 3D resolution and field of view (FOV) are ~30 nm and ~30 µm, respectively (Liu *et al.*, 2011; Ge *et al.*, 2018). Thus, mosaic processing is required when the sample is larger than the FOV. This process is inevitably sensitive to mechanical errors, which result in incomplete CT images. An FOV of ~100 µm was achieved with ~100 nm resolution in specific optical systems using a grating condenser (Stampanoni *et al.*, 2011; Rau *et al.*, 2017; Wang *et al.*, 2018; Kaira *et al.*, 2019). In these systems, ~100 µm FOV can be realized; however, it is difficult to obtain CT images of 100 µm samples due to the limitation of the depth of focus (DOF) of the objective zone plate.

In this study, we propose a simple way to enlarge the FOV of TXM-CT without coherent X-rays and condenser optics, which delivers a 400 µm FOV and Zernike phase-contrast images at below 500 nm resolution. Because of its simplicity, it can be applied to both synchrotron and laboratory sources.

2. General concept

A full-field TXM is typically composed of condenser optics, an objective zone plate, a phase plate, scintillator, objective lens and detector. A glass capillary or grating functions as the condenser optics, which collect the X-rays in the form of a hollow cone and focuses it onto the sample. The focused light generates image information as it passes through the sample, and is magnified by the zone plate. The ratio between the numerical apertures (NA) yields the coherent factor $L = \mathrm{NA}_{\mathrm{condenser}}/\mathrm{NA}_{\mathrm{zoneplate}}$. The resolution of the system is defined as $R = S(L)\lambda/\mathrm{NA}_{\mathrm{zoneplate}}$, where $S(L)$ is the degree of coherence and equals 0.58 ($L \simeq 1.2$) to 0.82 ($L = 0$), and λ is the wavelength of light (Born & Wolf, 2013). Combined with the zone plate equation $\mathrm{NA} = \lambda/2\Delta r$, the resolution can be simplified to $R = 1.16\Delta r$ ($L \simeq 1.2$), $R = 1.22\Delta r$ ($L = 1$) and $R = 1.64\Delta r$ ($L = 0$). Here, Δr is the outermost zone width of the zone plate. Although the TXM method offers the advantage of obtaining a uniform image at high resolution, its application to large size samples is limited. The applicable sample size (*i.e.* the FOV) is defined by the focused beam size on the sample plane. The sample should be moved and several images have to be stitched when the sample size is larger than the FOV. Such a stitching method produces an uneven background (Kyrieleis *et al.*, 2009; Andrews *et al.*, 2010; Wang *et al.*, 2015). Additionally, moving the rotational axis of the sample to obtain 3D images inevitably causes a driving error, thereby degrading the resolution. Thus, it is difficult to acquire CT images of large volumes using conventional TXM-CT and stitching.

Here, we propose a way to enlarge the FOV of TXM-CT. Fig. 1(*a*) illustrates the basic principles of the large-volume TXM-CT (LV-TXM-CT). A key feature of this method is that the collimated light is used without the condenser to extend the FOV as the diameter of the zone plate. When a sample is irradiated with a well defined collimated beam, its magnified image is formed on the detector based on the same principle as that of a simple magnifying glass. However, the zeroth-order beam transmitted through the zone plate and higher-order images are simultaneously displayed due to the diffraction characteristics of the zone plate. Thus, a large FOV can be realized if all beams except the +1st order beam are blocked. In our study, two beam stoppers were used, and a large FOV image (A3) was obtained by stitching together two semi-circular images (A1 and A2). As there is no motion except for sample rotation, the 3D resolution is only affected by the rotational motion error.

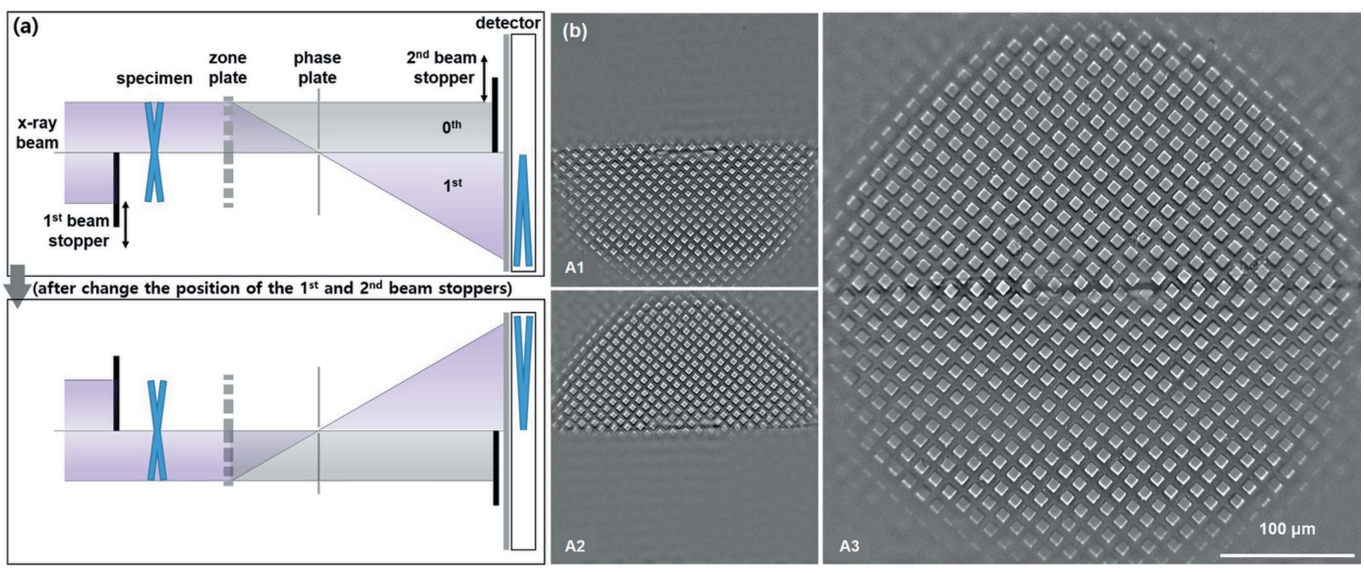

Figure 1
(*a*) Schematic layout for large-volume full-field X-ray nanotomography. (*b*) Example of a copper mesh sample. Half of the two images (A1 and A2) are extracted and then stitched together (A3).

The proposed method is an off-axis illumination (OAI) technique when $L = 0$ ($NA_{condenser} = 0$). TXM using OAI method has already been studied both theoretically and experimentally (Lee *et al.*, 1995; Takeuchi *et al.*, 2002). The resolution is therefore $1.64\Delta r$ at the optical axis but is in fact $0.82\Delta r$ because $NA_{zoneplate}$ is doubled at the edge, as reported in a previous study (Lim *et al.*, 2013). Though the resolution varies by a factor of two depending on the location, an ~100 nm resolution can still be achieved over the entire FOV if $\Delta r = 100$ nm. It should be noted that, in some regions, the resolution is better compared with the case of a typical TXM setup, *i.e.* $L = 1$ ($R = 1.22\Delta r$).

The Zernike phase-contrast method can be used to improve the image contrast. This can be achieved by installing a phase plate (a thin metal film) with a micrometre-sized hole at the back focal plane of the zone plate. A quarter-wavelength phase delay between the transmitted (zeroth order) and scattered light (higher orders) is generated, resulting in Zernike phase contrast. However, a sideband artifact appears because most of the illumination is not on the optical axis. Laterally shifting the illumination to a single side enables higher orders of scattered light to be collected by the zone plate, contributing to image formation. The other side tends to miss all the higher-order scattered light. This ensures constructive and destructive interference between the zeroth order and higher orders, producing a pseudo 3D appearance in the image. This phenomenon becomes noticeable as the sample is moved away from the optical axis. The sideband artifact and Zernike phase contrast only affect the periphery and interior of the sample image, respectively. Although the artifact slightly degrades the image resolution, most of the FOV is not significantly affected. We will discuss this aspect further with an example in Section 3.

LV-TXM-CT can be realized by acquiring the transmission images while rotating the sample, similar to a conventional TXM-CT. If a conventional TXM-CT obtains $(50\ \mu m)^3$ of volume information, then in comparison the LV-TXM-CT can at the same time obtain $(400\ \mu m)^3$, which is 500× greater. In CT imaging, the depth of focus (DOF) is a factor that should be considered. In general, the DOF is simply defined as $\sim 4\Delta r^2/\lambda$ based on the zone plate and wavelength. For example, if the energy of light is 12.4 keV ($\lambda = 0.1$ nm) and $\Delta r = 100$ nm, the DOF is ~400 µm. Thus, it can be seen that LV-TXM-CT with an FOV of 400 µm can be easily realized when using hard X-rays. There have been in-depth studies on the DOF in scanning transmission X-ray microscopy (STXM) (Maser *et al.*, 2000), but no quantitative study has reported the resolution degradation when a sample is out of the DOF in conventional TXM-CT. We will discuss this in detail in the following section.

3. Proof of concept

The LV-TXM-CT experiment was conducted at the BL7C spectroscopic X-ray Nano Imaging beamline (sXNI) at the Pohang Light Source-II (Lee *et al.*, 2017). Bright X-rays were generated using an in-vacuum undulator and monochromatic X-rays of 6.36 keV were then selected using a liquid-nitrogen-cooled double-crystal monochromator (DCM). Diverging X-rays were focused on the sample using bendable horizontal and vertical focusing plane mirrors. In this experiment, the mirrors were bent to collimate the beam. A tungsten objective zone plate with an 80 nm outermost zone width, 400 µm diameter and 1 µm thickness (made by Zoneplates Ltd) was used for imaging. A scintillator-coupled optical microscope composed of thin scintillation crystals (15 µm-thick Tb:LSO) with a 20× optical objective and large-area optical CCD (U16MF, Apogee) composed of 4096 × 4096 sensors with 9 µm square pixels functioned as the detector. The X-ray energy was fixed at 6.36 keV to obtain Zernike phase contrast using a holed aluminium-film phase plate of 3.78 µm thickness. The diameter of the hole was 20 µm. A high-precision air-bearing rotation stage (RT150U, made by Lab Motion Systems) was used for CT imaging. CT images were obtained using the filtered back-projection method, and the 3D volume images were rendered using 3D imaging software (Avizo, Visualization Sciences Group). When collimated X-rays pass through the zone plate, +*n*th-order diffracted beams are focused in the direction of the optical axis (here, we consider only zeroth-order and +1st-order beams). The postive first-order diffracted beams obey the lens-maker formula, having an efficiency of less than ~10%. However, the zeroth-order beam transmitted at ~60% efficiency is directed to the detector. Thus, the zeroth-order beam must be securely blocked to precisely measure a relatively weak positive first-order diffracted beam. For this purpose, two beam-stoppers are used. The beam-stopper in front of the sample cuts the beam into a semicircle [first beam-stopper in Fig. 1(*a*)] and produces a collimated semicircular light beam. The second beam-stopper located immediately in front of the scintillator blocks the transmitted zeroth-order beam so that only the +1st-order diffracted beam is directed to the detector. The edge of each beam-stopper is located at the centerline of the zone plate, thus preventing the transmission of the zeroth-order beam. As the undulator radiation from the synchrotron source is composed of partially coherent light, edge diffraction occurs when it passes through the edge of the beam-stopper. A thin gold film (thickness = 25.4 µm, transmittance = 1.2×10^{-5} % at 6.36 keV) was used as a beam-stopper by laser cutting the edge to minimize edge diffraction and scattering. Fig. 1(*b*) shows a mesh image with a period of 12.5 µm and an FOV with a diameter of 400 µm. A1 and A2 represent the normalized images of the raw data showing half the sample, while A3 is the stitched image. A closer observation indicates that the out-of-focus +2nd-order diffraction image appears faint in the regions outside the FOV, but has no significant effect on the +1st-order diffracted image as it is weak (<1%) and defocused. A small part of the image appears overexposed at the center, as the zeroth-order beam passes through a fine gap between the edges of the two beam-stoppers. It makes an artifact-like distorted image in the center of the image. Though there are minor issues to be resolved, we confirmed that an acceptably even image is produced within the entire FOV.

We first imaged a resolution test target to quantify the resolution based on the position (Fig. 2). The width of the Siemens pattern at the center of the target is 30 nm to 480 nm. The resolution was checked by measuring the pattern at various positions. Patterns larger than ~200 nm can be distinguished when located in the center of the FOV. The zone plate used in the experiment has Δr = 80 nm, which implies that the expected resolution is ~100 nm. However, an ~200 nm resolution at the center is reasonable, as the effective pixel size is Δp = 98 nm due to the limited pixel size of the detector. Fig. 2(*b*) shows a pseudo-color image of the interpolated resolution measured at different points. The *x* and *y* axes are the coordinates in the sample plane. Fig. 2(*c*) shows the power spectra (azimuthally averaged) at three different positions (P1, P2 and P3) along the *y* axis. The highest resolution can be observed at the center, while the resolution is up to two times lower when we move away from the center. An isotropic trend is seen along the radial direction. Interestingly, this result is the exact opposite of what we expected (the resolution at the center is two times lower than the resolution at the edges). As described in a previous study (Lim *et al.*, 2013), OAI imaging presents a more prominent resolution difference between the horizontal and vertical directions as the sample moves away from the optical axis [Fig. 2(*d*)]. It is true that using OAI imaging helps to increase the resolution in 1D but introduces aberration and sideband artifacts, which effectively lower the resolution in the 2D image. This aspect has also been reported in OAI lithography (Benk *et al.*, 2015). As a result, in the middle of the FOV (within a diameter of ~200 µm = half the diameter of zone plate), the resolution of the system is reasonable (in the range 200–300 nm) and determined by the effective pixel size (because $\Delta p > \Delta r$), but gradually decreases in the outer part. The resolution within the FOV is not uniform and ranges from 200 nm to 500 nm, but is sufficient to characterize the sub-micrometre-sized features.

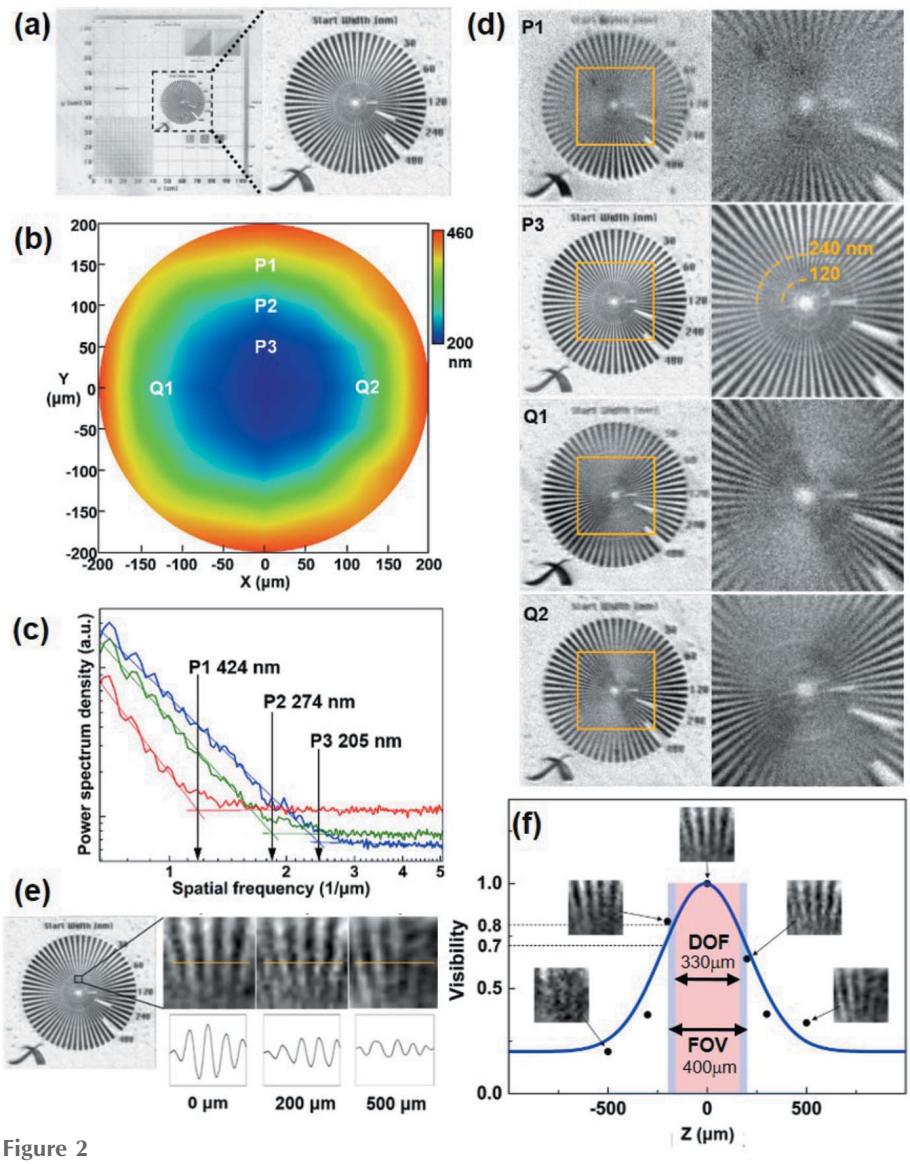

Figure 2
2D resolution characteristics using (*a*) a resolution test pattern. (*b*) Pseudo-colored resolution distribution, (*c*) power spectrum density and (*d*) Siemens target images at different positions in the FOV. (*e*,*f*) DOF evaluation based on the visibility of line plots of Siemens targets with respect to the defocus distance.

The DOF is an important limitation for volumetric reconstructions in CT imaging because it is smaller than the FOV in a typical TXM. To quantitatively determine the DOF of the LV-TXM-CT, the visibility [= $(I_{max} - I_{min})/(I_{max} + I_{min})$] of the target pattern was measured while scanning ±500 µm from the focus position along the optical axis [Fig. 2(*e*)]. Following the Gaussian fitting of the measured values, a DOF ≃ 330 µm was obtained by measuring the width corresponding to 80% visibility [Fig. 2(*f*)]. This is significantly different from the generally accepted theoretical value (DOF = $4\Delta r^2/\lambda$ = 132 µm) in our case, as we are considering the DOF of the focused beam with respect to uniform plane-wave illumination. In optical microscopy, Berek derived a formula that takes the magnification into account, which has subsequently been modified in various ways (Berek, 1927). There have also been in-depth studies on the DOF in STXM. They showed experimentally that the DOF is $\sim 4.88\Delta r^2/\lambda$ (Maser *et al.*, 2000). According to the equation, its theoretical value (322 µm) is in agreement with our experimental value. Thus, a slightly lower resolution is expected at the sample edge when considering a 400 µm-thick sample.

The 3D resolution of the LV-TXM-CT was experimentally determined by imaging a test sample. The resolution

test sample consists of copper powders and silica particles of 10 µm and 1 µm size, respectively, which were randomly packed in a 300 µm-diameter borosilicate capillary. Fig. 3(*a*) shows the volume-rendered image of the sample and Figs. 3(*b*) and 3(*c*) show the randomly selected slice images. According to the Crowther criterion (Crowther *et al.*, 1970), $N \simeq \pi D/d$, where N is the number of projection images required for full Fourier domain sampling to reconstruct a 3D object of size D at an isotropic spatial resolution d. Thus, for a 400 µm sample, 3140 projection images are required to obtain a 3D image at 400 nm resolution. In this experiment, 3600 projection images were captured for a 400 µm (H) × 200 µm (V) FOV (*i.e.* we used one semicircle illumination) from 0° to 180°. The copper powders were clearly visible without any motion error correction due to a high-precision air-bearing rotation stage, which has an error <100 nm along both the rotational and the vertical directions. In contrast, images of the silica particles and capillary were slightly faint. Copper experiences a 40× greater phase delay than silica due to differences in the refractive index (×4) and thickness (×10) at E = 6.36 keV. This phase difference causes contrast differences in the Zernike phase-contrast image. The slice images show randomly packed silica, copper powders and empty space. The sideband artifacts, which were not visible in copper powder at the center [Fig. 3(*b*2)], are clearly visible at the capillary rim [Fig. 3(*c*2)]. These pseudo 3D appearances are visible at the periphery of the copper powder in the outer parts of the FOV, while the Zernike phase contrast appears inside the silica and copper powder in the entire FOV. The artifact depends on the size and refractive index of the sample. When we closely observe the aggregated silica in the outer parts of the FOV, the 3D appearance is rarely visible and does not severely degrade the image quality [Fig. 3(*d*)]. As a common resolution metric, Fourier ring correlation (FRC) is used to quantify the reproducibility of the frequency content of the image spectrum (Heel & Schatz, 2005). Choosing the threshold corresponding to an average information content of 1/2 bit per pixel, the FRC indicates estimated resolutions of 204 nm and 310 nm, depending on the positions [Fig. 3(*e*)]. As with 2D resolution, 3D resolution also decreases with increasing distance from the rotational axis. Considering that the sample is 300 µm in size, these values are consistent with the 2D resolution [Fig. 2(*b*)]. Thus, within at least 300 µm FOV, we can conclude that the artifact does not significantly overshadow the advantages offered by the large FOV 3D images.

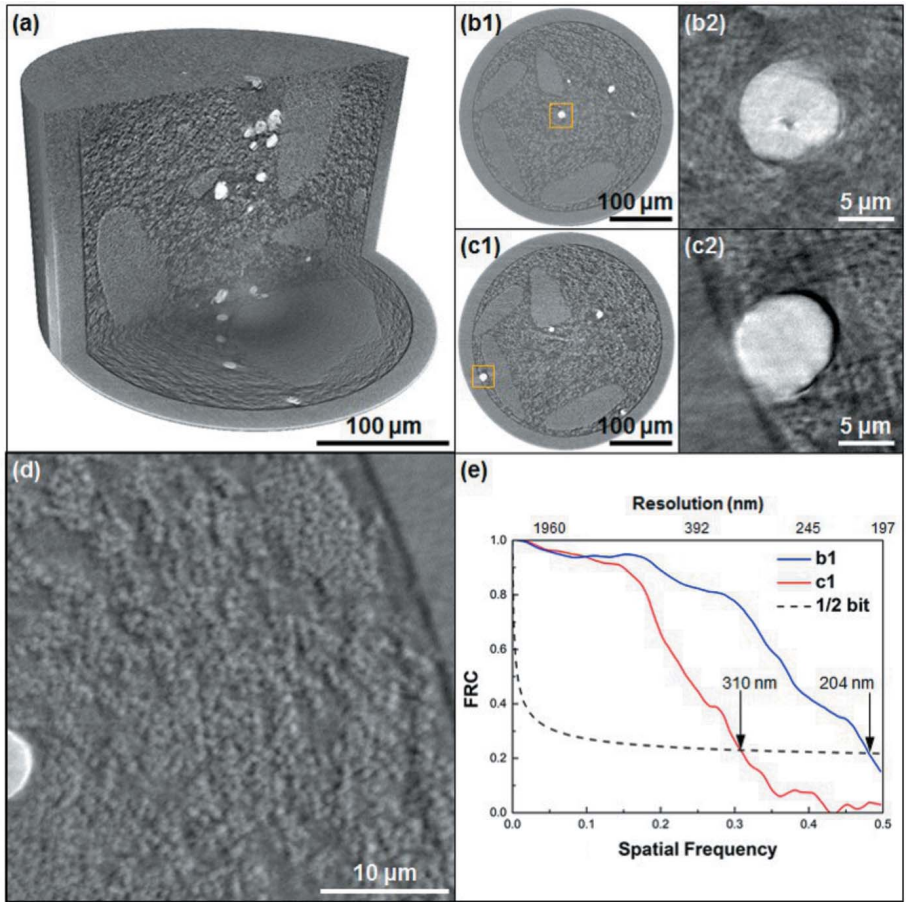

Figure 3
3D resolution evaluation. (*a*) Volume-rendered image of the 1 µm silica and 10 µm copper powders in a capillary. (*b*)–(*c*) Reconstructed slice images and enlarged images of copper powders. (*d*) Enlarged image of silica particles aggregated at the rim of a capillary. (*e*) Estimation of the resolution at different positions [yellow region in (*b*1) and (*c*1)] using the Fourier ring correlation method.

4. Practical applications

We demonstrate the general applicability of the LV-TXM-CT system using practical samples having sub-millimetre-sized nanostructures. The first sample is the integrated circuit (IC) microchip, which is often used as an X-ray microscopic sample because it has well defined metal nano-structures. The metrology of microchips, wherein billions of circuit elements are arrayed in precise patterns, is a major challenge for manufacturers who need to verify which fabrication lines come off and how they should be designed. Recently, the 3D nanostructure of a microprocessor has been visualized at 15 nm resolution using X-ray ptychography; however, its FOV is limited to 10 µm (Holler *et al.*, 2017). In this experiment, we extracted a part of the Pentium 4 processor (630, Prescott) fabricated by the Intel Corporation. This was manually extracted to obtain a large sample, due to which the sample does not appear clean in the optical microscopic image. A total of 1800 projection images (rotation angle steps of 0.2°) were acquired, each with an exposure time of 10 s. The effective pixel size was 90 nm. The processor is fabricated using a fine linewidth of 90 nm. Fig. 4(*a*) shows the

CT image of the microchip for a size and depth of ∼360 µm and ∼17 µm, respectively. It has five layers of electrical wires, which results in a complex volume image [Fig. 4(*a*)]. Fig. 4(*b*) shows the depth images of each layer from the top (L1) to the bottom (L5). The linewidth of the wires varies from 3 µm to 300 nm. As expected, the finest wire of 90 nm was not resolved due to the limited resolution. Even though the images have a relatively low resolution, we believe that this is sufficient to visualize bulk structures and investigate the wiring and layer dimensions, interconnection failures, short circuits, defects and cracks.

We next considered the Artemia cyst sample, which is an attractive crustacean model with an ultrastructure in extremophile biology. The surface of the Artemia cyst has evolved to enable its survival in salt lakes with high pH, low oxygen levels, osmotic pressure, dryness and dramatic temperature changes. The key to survival is to remain dormant in the cyst for months until the optimal incubation conditions are met. Thus, the mechanism of cyst shell formation and its measurement is an interesting experiment. The shell structure containing aeropyles, alveoli, multi-lamellae and fibers has been uncovered using electron microscopy. In this experiment, an alive dormant Artemia cyst (brine shrimp) was placed in a thin capillary without staining, fixing or any pre-processing. Here, 900 projection images were acquired. The exposure time was set to 2 s to minimize thermal damage from radiation. The effective pixel size was increased to 360 nm to shorten the exposure time. Fig. 4(*d*) shows the 3D volume image of the Artemia cyst, with an optical microscopic image in the inset. The image shows that hundreds of embryos remain protected within the ∼10 µm-thick shell. The boundaries between the embryos are not clearly distinguished as they are surrounded by the liquid nutrient. Fig. 4(*e*) shows the enlarged cross-section of the shell that consists of a cortical layer (CL), an alveolar layer (AL) and cuticular membrane (CM). The cortical layer is composed of cuticulin which covers the outer surface. The alveolar layer – known to be composed of ∼360 nm pores that contain the brine for moisture retention, osmotic pressure balance or thermal insulation – is not resolved clearly in the CT image. However, the interlayer boundary could be clearly distinguished. It is important to note that the sample does not experience any damage because the X-rays are not focused on the sample plane, which results in a relatively small dose compared with conventional TXM-CT. This demonstrates that LV-TXM-CT with Zernike phase contrast can be used for imaging various soft samples such as biological specimens, polymers and liquid drops.

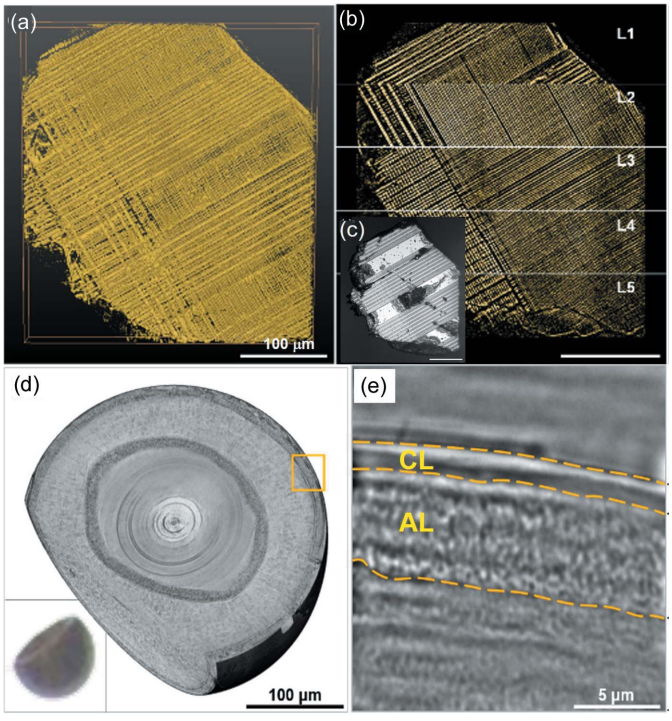

Figure 4
Application examples. (*a*) Volume-rendered image of an integrated circuit, (*b*) depth-specified images of each layer and (*c*) optical microscopic image. (*d*) Volume-rendered image of an Artemia cyst and the optical image (inset). (*e*) Enlarged cross-sectional image of a cyst shell.

5. Conclusions

We demonstrated a method for large-volume full-field transmission X-ray nanotomography, which delivers a 400 µm FOV and Zernike phase-contrast images at below 500 nm resolution. The simple setup can be easily incorporated in tube-source based projection X-ray CT and currently operational synchrotron-based TXM. Though there remain some issues (anisotropic resolution and artifacts) to be solved, this method is well suited for imaging research samples containing internal micrometre structures that are difficult to section or stain. This method increases the FOV of a typical TXM, but still corresponds to a ratio of ∼1000 between resolution and FOV. The current FOV and spatial resolution are determined by the camera and effective pixel sizes rather than by the zone plate, which can enable a 1 mm FOV at sub-100 nm resolution when using a large, high-definition camera. We believe that our proposed approach can used be used to explore areas previously unseen with projection-based X-ray CT, and can potentially expand the application fields of conventional TXM.

Funding information

This research was financially supported by Basic Science Research Program through the National Research Foundation of Korea (NRF), funded by the Ministry of Education (project: Development of a 3D X-ray vision machine to investigate nano-structures); the Ministry of Trade, Industry and Energy (MOTIE) (grant No. 10080526); Korea Semiconductor Research Consortium (KSRC: Program for the development of future semiconductor devicea); and National Research Foundation of Korea (NRF-2019R1A6B2A01081034).

References

Andrews, J. C., Almeida, E., van der Meulen, M. C., Alwood, J. S., Lee, C., Liu, Y., Chen, J., Meirer, F., Feser, M., Gelb, J., Rudati, J., Tkachuk, A., Yun, W. & Pianetta, P. (2010). *Microsc. Microanal.* **16**, 327–336.

Benk, M. P., Miyakawa, R. H., Chao, W., Wang, Y., Wojdyla, A., Johnson, D. G., Donoghue, A. P. & Goldberg, K. A. (2015). *J. Micro/Nanolith. MEMS MOEMS*, **14**, 013507.

Berek, M. (1927). *Ber. Ges. Naturw. Marburg*, **62**, 189–223.

Born, M. & Wolf, E. (2013). *Principles of Optics: Electromagnetic Theory of Propagation, Interference and Diffraction of Light.* Cambridge University Press.

Burg, S., Washington, A., Villanova, J., Dennison, A., Mcloughlin, D., Mykhaylyk, O., Vukusic, P., Furnass, W., Jones, R., Parnell, A. & Fairclough, J. (2020). *Sci. Data*, **7**, 163.

Cheng, Y., Suhonen, H., Helfen, L., Li, J., Xu, F., Grunze, M., Levkin, P. & Baumbach, T. (2014). *Soft Matter*, **10**, 2982–2990.

Cloetens, P., Ludwig, W., Baruchel, J., Van Dyck, D., Van Landuyt, J., Guigay, J. & Schlenker, M. (1999). *Appl. Phys. Lett.* **75**, 2912–2914.

Crowther, R., DeRosier, D. & Klug, A. (1970). *Proc. R. Soc. London. A*, **317**, 319–340.

Ferstl, S., Schwaha, T., Ruthensteiner, B., Hehn, L., Allner, S., Müller, M., Dierolf, M., Achterhold, K. & Pfeiffer, F. (2020). *Sci. Rep.* **10**, 3960.

Ge, M., Coburn, D., Nazaretski, E., Xu, W., Gofron, K., Xu, H., Yin, Z. & Lee, W. (2018). *Appl. Phys. Lett.* **113**, 083109.

Heel, M. van & Schatz, M. (2005). *J. Struct. Biol.* **151**, 250–262.

Holler, M., Guizar-Sicairos, M., Tsai, E., Dinapoli, R., Müller, E., Bunk, O., Raabe, J. & Aeppli, G. (2017). *Nature*, **543**, 402–406.

Kaira, C., Stannard, T., De Andrade, V., De Carlo, F. & Chawla, N. (2019). *Acta Mater.* **176**, 242–249.

Kyrieleis, A., Ibison, M., Titarenko, V. & Withers, P. (2009). *Nucl. Instrum. Methods Phys. Res. A*, **607**, 677–684.

Larsson, D., Vågberg, W., Yaroshenko, A., Yildirim, A. & Hertz, H. (2016). *Sci. Rep.* **6**, 39074.

Lee, H., Anderson, E., Da Silva, L. & Trebes, J. (1995). *AIP Conf. Proc.* **332**, 543–548.

Lee, S., Kwon, I., Kim, J.-Y., Yang, S.-S., Kang, S. & Lim, J. (2017). *J. Synchrotron Rad.* **24**, 1276–1282.

Lim, J., Park, S., Huang, J., Han, S. & Kim, H. (2013). *Rev. Sci. Instrum.* **84**, 013707.

Liu, Y., Andrews, J. C., Wang, J., Meirer, F., Zhu, P., Wu, Z. & Pianetta, P. (2011). *Opt. Express*, **19**, 540–545.

Martínez-Criado, G., Villanova, J., Tucoulou, R., Salomon, D., Suuronen, J.-P., Labouré, S., Guilloud, C., Valls, V., Barrett, R., Gagliardini, E., Dabin, Y., Baker, R., Bohic, S., Cohen, C. & Morse, J. (2016). *J. Synchrotron Rad.* **23**, 344–352.

Maser, J., Osanna, A., Wang, Y., Jacobsen, C., Kirz, J., Spector, S., Winn, B. & Tennant, D. (2000). *J. Microsc.* **197**, 68–79.

Müller, M., de Sena Oliveira, I., Allner, S., Ferstl, S., Bidola, P., Mechlem, K., Fehringer, A., Hehn, L., Dierolf, M., Achterhold, K., Gleich, B., Hammel, J. U., Jahn, H., Mayer, G. & Pfeiffer, F. (2017). *Proc. Natl Acad. Sci. USA*, **114**, 12378–12383.

Pfeiffer, F., Weitkamp, T., Bunk, O. & David, C. (2006). *Nat. Phys.* **2**, 258–261.

Rau, C., Bodey, A., Storm, M., Cipiccia, S., Marathe, S., Zdora, M., Zanette, I., Wagner, U., Batey, D. & Shi, X. (2017). *Proc. SPIE*, **10391**, 103910T.

Reichardt, M., Frohn, J., Khan, A., Alves, F. & Salditt, T. (2020). *Biomed. Opt. Expr.* **5**, 2633–2651.

Stampanoni, M., Marone, F., VilaComamala, J., Gorelick, S., David, C., Trtik, P., Jefimovs, K. & Mokso, R. (2011). *AIP Conf. Proc.* **1365**, 239–242.

Takeuchi, A., Uesugi, K., Takano, H. & Suzuki, Y. (2002). *Rev. Sci. Instrum.* **73**, 4246–4249.

Wang, H., Wang, J., Chen-Wiegart, Y. & Kent, D. (2015). *Proc. Natl Acad. Sci. USA*, **112**, 12598–12603.

Wang, Y., Ren, Y., Zhou, G., Du, G., Xie, H., Deng, B. & Xiao, T. (2018). *Nucl. Instrum. Methods Phys. Res. A*, **896**, 108–112.

Wenz, J., Schleede, S., Khrennikov, K., Bech, M., Thibault, P., Heigoldt, M., Pfeiffer, F. & Karsch, S. (2015). *Nat. Commun.* **6**, 7568.